J Solid State Electrochem (2011) 15:2523–2544
DOI 10.1007/s10008-011-1465-x

REVIEW

Composition depth profile analysis of electrodeposited alloys and metal multilayers: the reverse approach

Katalin Neuróhr · Attila Csik · Kálmán Vad · András Bartók · György Molnár · László Péter

Received: 6 April 2011 / Revised: 2 June 2011 / Accepted: 7 June 2011 / Published online: 23 June 2011

Abstract The reverse depth profile analysis is a recently developed method for the study of a deposit composition profile in the near-substrate zone. The sample preparation technique enables one to separate the deposit and a thin cover layer from its substrate, and the initial roughness of the sample is much smaller than in the conventional sputtering direction. This technique is particularly suitable to study the zones being formed in the early phase of the electrodeposition of alloys. It has been demonstrated with the reverse depth profile analysis that in many cases when one component of an alloy is preferentially deposited, an initial zone is formed that is rich in the preferentially deposited component. This phenomenon is demonstrated for Ni–Cd, Ni–Sn, Fe–Co–Ni, Co–Ni, and Co–Ni–Cu alloys. The composition change is confined to the initial 150-nm-thick deposit, and it is the result of the interplay of the deposition preference and the depletion of the electrolyte near the cathode with respect to the ion reduced preferentially. The reverse depth profile analysis made it possible to compare the measured and the calculated composition depth profile of electrodeposited multilayers. It has been shown that the decay in the composition oscillation intensity in Co/Cu multilayers with the increase of the sputtering depth can be derived from the roughness measured as a function of the deposit thickness.

Keywords Electrodeposition · Depth profile analysis · Alloy formation · Multilayers

K. Neuróhr · A. Bartók · L. Péter (✉)
Research Institute for Solid State Physics and Optics,
Hungarian Academy of Sciences,
1525 Budapest P.O. Box 49, Hungary
e-mail: lpeter@szfki.hu

A. Csik · K. Vad
Institute of Nuclear Research, Hungarian Academy of Sciences,
4001 Debrecen P.O. Box 51, Hungary

G. Molnár
Research Institute for Technical Physics and Materials Science,
Hungarian Academy of Sciences,
1525 Budapest P.O. Box 49, Hungary

Present Address:
A. Bartók
Laboratoire de Génie Electrique de Paris, Université Paris Sud,
Orsay , France

Introduction

Summary of the depth profile analysis methods

For all objects whose surface composition differs from the bulk one, the question may arise how the functionality of the surface layer is related to the in-depth variation of the layer composition. The study of the composition variation of a surface layer with a thickness of typically less than 100 μm is a special field of analytical chemistry, which is called the depth profile analysis (DPA). In the sections below, the methods of composition depth profile analysis are summarized.

Non-destructive methods

The non-destructive methods are summarized in Fig. 1. Two of the methods applying electromagnetic radiation, X-ray reflectometry (XRR) and ellipsometry, have the disadvantage that a priori information should be used for a model calculation, the result of which has to be compared with the data measured. Both above-mentioned

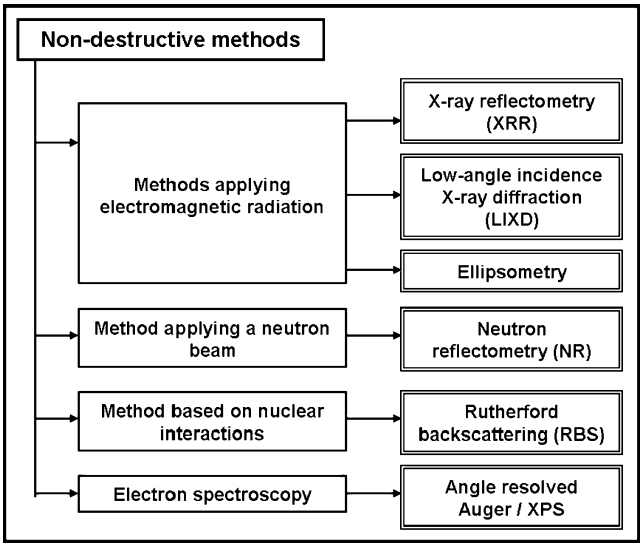

Fig. 1 Classification of the depth profile analysis methods: non-destructive methods

methods can be used primarily for the analysis of layered systems, and graded composition changes can rather be modeled by taking into account several consecutive layers, each of them assumed to be homogeneous. The sensitivity of these methods to the surface roughness is drastically different. While XRR is very sensitive to the undulation of the layer interfaces at the nanometer scale, the critical roughness scale of the ellipsometry is related to the wavelength of the light used. The analysis depth of both methods is at most a few tens of nanometers. Neutron reflectometry (NR), being also a scattering technique, works on the same principle as XRR but has a different sensitivity range in the reciprocal space.

Low-angle incidence X-ray diffraction (LIXD) has the advantage that no a priori information is needed to evaluate the results since the scattering vector of the X-ray is the same as in conventional X-ray diffractometry. The incidence depth of the X-ray can be tuned with the incidence angle, hence focusing on either the topmost atomic layers at low incidence angle or obtaining information on a wider surface zone at higher incidence angle. The LIXD method is obviously sensitive to the crystallinity of the samples and has the usual restriction of relative sensitivity as other diffraction-based methods.

In contrast to the methods based on electromagnetic radiation, Rutherford backscattering (RBS) is suitable for the analysis of surface layers with continuously varying composition and with a fairly large depth. Here, the disadvantage is the very high demand of instrumentation. The intensity spectrum of the backscattered particles is to be compared with a simulation, although the information needed for the simulation for the RBS spectra is less than for other non-destructive methods because the characteristic energy of the particles after the reflection on a particular nucleus is known. An important advantage is that the lateral inhomogeneity of the sample is not a problem, and even laterally structured heterogeneous materials can also be studied by RBS. This feature of RBS is quite unique among the DPA methods. The depth resolution that can be achieved with RBS is several nanometers, and the information depth strongly depends on both the atomic number of the specimen analyzed and the nature and energy of the particles scattered.

Finally, it has to be noted that electron spectroscopy methods like Auger electron spectroscopy (AES) and X-ray photoelectron spectroscopy (XPS) can also be used as non-destructive DPA methods in the angle resolved mode. The information depth for these methods is defined as the thickness of the topmost layer producing 95% of the total intensity. This depth can range from about 2–3 to 8–10 nm, or in the case of hard X-ray photoelectron spectroscopy to 20–30 nm. The information depth also depends on the incidence angle and energy of the ionization beam, on the angle of escaping electrons, and on the material studied. Other features of these methods will be discussed in the next section together with the other related methods based on sample sputtering.

The main advantage of the non-destructive methods is in general the repeatability of the study on the very same specimen. This is true for XRR and ellipsometry, but for RBS one has to consider the radiation damage of the sample after a long exposure to ions of typically a few MeV energy. In special cases, the non-destructive methods can be used even in situ.

Destructive methods

The hierarchical diagram of the destructive depth profile analysis techniques is shown in Fig. 2. These are all ex situ methods.

The block of cross-sectional sampling techniques includes methods that can be repeatedly used for a particular specimen after the appropriate sample preparation. The lateral resolution of AES can be as low as 25 nm, and this convolution length determines how much a linescan is expected to be smeared out. Repeated analysis for the same area of the sample is possible, similarly to the non-destructive methods.

The DPA methods based on sputtering of the samples with an ion beam are by far the most popular. When the new surface left behind after a sputtering step is analyzed, DPA is carried out via the analysis of the composition of the surface, and the consecutive removal of the surface layers makes it possible to reveal the in-depth composition profile. With these methods, chemical information can also be obtained if the sputtering itself does not change the

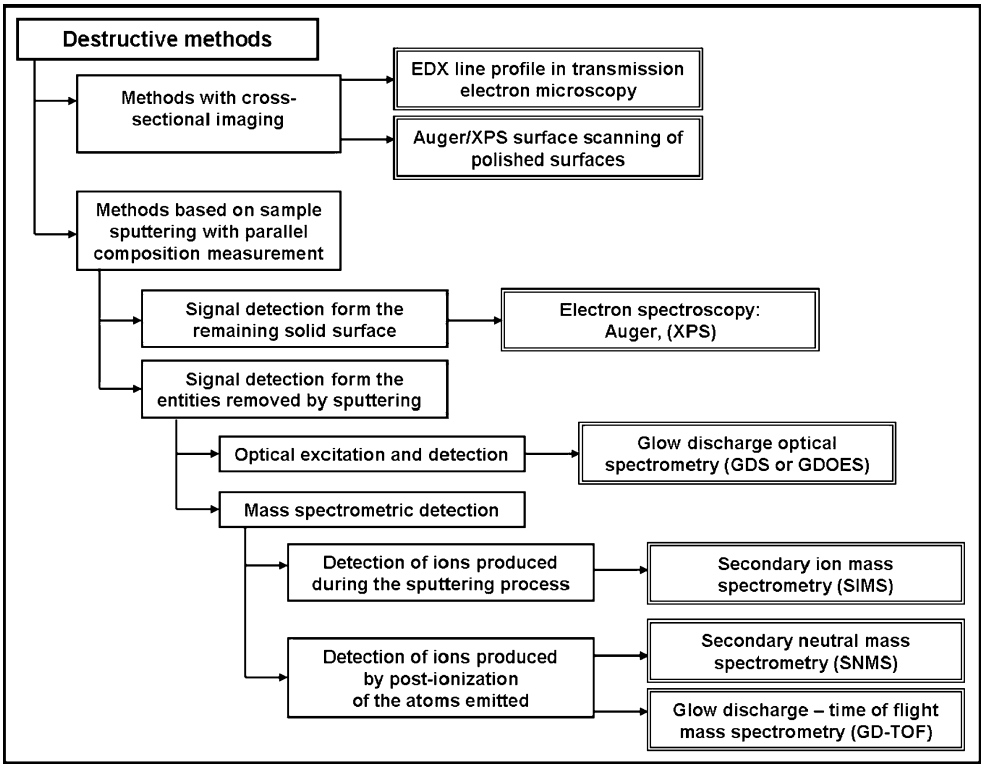

Fig. 2 Classification of the depth profile analysis methods: destructive methods

chemical nature of the specimen. It is also a prerequisite of the analysis of the chemical state that the contamination of the high-vacuum system does not impact significantly the surface composition within the analysis time. It is always a problem with sputtering-based methods that preferential sputtering may occur, and the composition of the surface analyzed may significantly differ from the composition of the actual layer of the specimen before the sputtering.

AES and XPS are very similar; they differ mostly in the ionization mode and the electron escape mechanism. In the case of both methods, the calculation of the sputtering depth from the sputtering time can be made by the measurement of sputtering rates, and the conversion of the detected intensities to molar fractions needs calibration standards due to the different detection probability of elements.

In some destructive methods, the ionic state of atoms (or occasionally clusters) providing the signal for the analysis is produced in a separate step after the emission from the surface. The majority of sputtered particles are atoms, not ions. The "after-treatment" of the emitted entities (excitation in glow discharge optical emission spectrometry (GDOES) or post-ionization in secondary neutral mass spectrometry (SNMS)) makes it possible that the analysis does not need to rely on the population of species (atoms, ions) produced by the sputtering itself. Instead, essentially all atoms can be involved into the analysis. Therefore, the matrix sensitivity of the DPA is practically entirely eliminated. In contrast, for the secondary ion mass spectrometry (SIMS), the ion yield in the sputtering steps remains below 1% of all emitted entities. Hence, the composition of the ionic fraction cannot be representative for the entire emitted population, and the calculation of the molar fraction from the SIMS ion intensities detected is very cumbersome.

Although the methods in which the emitted particles are analyzed do not yield any chemical information of the solid sample, they are more suitable for a trace element analysis even at the ppm level. A special target of analysis is the hydrogen atom which can be detected the most conveniently by using mass spectrometry.

Application of various DPA methods in electrochemistry

The recent literature of the DPA in electrochemical studies is summarized in Table 1. The list is confined for cases where real in-depth composition analysis or species identification was carried out, but no work related to the overall composition analysis with a method otherwise appropriate for DPA is mentioned. Since materials of importance in electrochemistry have a great variety, the list intends to give a classification based primarily on the sample composition, and special aspects of the particular work are shortly mentioned as a remark. A logical classification of the works is particularly difficult because the DPA of electrodeposited materials is seldom the main goal of a study; rather, DPA is mostly used as an auxiliary method only for sample characterization.

Table 1 A representative literature summary on the DPA studies of materials prepared or modified with electrochemical methods (1990–2011)

Classification	Material	DPA method(s) used	Most important aspect of DPA in the work and other remarks	Reference
Study of the underpotential deposition	I_2	RBS	In situ detection of the accumulation of an iodine adlayer on gold electrode with a coverage of about 1.3-nmol/cm^2 level	[1]
	Ag	XPS, ARXPS	Underpotential deposition of Ag on Pt with the detection of S, O, and C as elements being also present at the surface	[2]
Metal deposits: one single main component	Cd	SIMS	Dependence of the hydrogen accumulation at the electroplated Cd/steel interface on the annealing conditions	[3]
	Cu	SIMS	S and Cl impurities show a local stability at their incorporation sites, whereas C is capable to segregate at room temperature; annealing leads to a segregation of S, too	[4]
	Cu	SIMS	Detection of most of the organic inclusions in the interfacial zones when there was a change in the plating process	[5]
	Pt/C	EDX linescan	Composition depth profiles of variously treated catalytic Pt layers on C	[6]
	Ru, Pd, Au	SIMS, XPS	On Ni substrate, Ru deposit yields a sharp interface, but a significant intermixing of Au and Pd with the substrate was found	[7]
Metal deposits: alloys	Cu–Sn	Scanning Auger microscopy	Detection of the oscillation of deposit composition accompanying the current oscillation during potentiostatic deposition	[8]
	Cu–Sn	SIMS	Calculation of the time needed to form an initial transition zone by using the Sand equation during Cu–Sn codeposition	[9]
	Co–Mo	AES, XPS	Identification of Mo oxides in the initial phase of the alloy deposition	[10]
	Co–W–P	AES	Detection of a phosphorous-rich zone near the substrate and lack of O in the bulk deposit	[11]
	Co–B, Co–W–B, and Co–W–B–P	AES	Improvement of corrosion resistance of Cu by a covering Co alloy layer	[12]
	Ni–W (amorphous)	Scanning Auger microscopy, EDX linescan	Detection of a Ni-rich zone in the near-substrate region of ED Ni–W alloys	[13]
	Ni–P, Ni–W, and Co–W	AES	Detection of the oscillation of the local alloy composition caused by the potential oscillation during galvanostatic deposition	[14]
	Ni–P	GDOES	Observation of compositional non-uniformity and its correlation with the amorphous-crystalline transition	[15]
	Ni–Fe	SIMS	Observation of a mesoscale layer structure in electrodeposited nanocrystalline Ni–Fe alloys	[16]
	Ni–Fe	XPS, AES, SIMS	Diffusion of the Cu substrate layer onto the top of the Ni–Fe deposit	[17]
	Ni–Fe alloy with Mo and Cr doping	SIMS	Impact of the alloying Cr and Mo on the accumulation and migration of Cu in Ni–Fe deposits	[18]
	Ni–Zn	GDOES, AES	A GDOES study with NiZn electrogalvanized layer as a model material	[19]
	Fe–Co–Ni	SNMS	Observation of the spontaneous near-substrate composition modulation in ED Fe–Co–Ni alloys	[20]
	Fe–Co–Ni	SNMS	Detailed analysis of the composition evolution of ED Fe–Co–Ni alloys	[21]
	Fe–Ga	XPS	Importance of substrate preconditioning on the Fe/Ga ratio, the oxygen content and the in-depth component distribution	[22]

Table 1 (continued)

Classification	Material	DPA method(s) used	Most important aspect of DPA in the work and other remarks	Reference
	Fe–Pt	AES	Decrease of oxygen content of the deposit and diffusion of the Cu substrate into the Fe–Pt layer upon annealing in hydrogen; confirmation of the even Fe and Pt distribution in the deposit	[23]
	Pd–Ag	AES	Decrease of the surface segregation of Ag as a result of hydrogen charging/discharging	[24]
	Pt–Cu, Pt–Ni, and Pt–Co layers	AES	Galvanic displacement of various metals by Pt and the resulting depth profiles	[25]
Metal deposits: nanostructures	Co/Cu multilayer	XPS	Confirmation of the layer structure of the samples	[26]
	NiCo/Cu multilayers	SNMS	Observation of the composition gradient formed during the Ni–Co codeposition at nanometer layer thicknesses	[27]
	Co–Cu/Cu multilayers	SNMS	Confirmation of the nominal depth profile of electrodeposited multilayers	[28]
	Co–Cu/Cu multilayers	SNMS	Application of surface roughness data for the evaluation of DPA measurements of nanoscale multilayers	[29]
	Co–Cu/Cu multilayers	SNMS	Demonstration of the advantage of the reverse depth profiling method for electrodeposited multilayers	[30]
	Ni, Co, and Co/Cu nanowires	RBS	Verification of the in-depth composition profile of the filled porous anodic alumina template under non-destructive conditions	[31]
	Ni nanowires	RBS	Verification of the in-depth composition profile of the filled porous anodic alumina template under non-destructive conditions	[32]
	Ni/Cu bilayers	XRR, NR	Confirmation of the layered structure, description of the morphology of buried Ni/Cu interface, measurement of the correlation length of the interfaces	[33]
Semiconductors	Bi_2Te_3	GDOES	Observation of a Te-rich layer near the substrate	[34]
	$CuInSe_2$	AES	Control of sample uniformity, detection of Se migration upon annealing	[35]
	$CuInSe_2$	AES	Identification of a Cu-rich bulk region and an In rich surface zone in ED $CuInSe_2$	[36]
	CdTe/ZnSe and CdTe/ZnTe bilayers	SIMS, LIXRD	Confirmation of the layered structure, exclusion of intermixing, validation of the LIXD results with SIMS measurements	[37]
	CdS/CdTe	RBS	Formation of an spatially limited, intermixed $CdTe_{(1-x)}S_x$ layer and the conversion of the whole CdS film into a $CdS_{(1-y)}Te_y$ layer upon annealing	[38]
	ZnO	SIMS	Control of the in-depth component distribution, correlation of the impurity level with the electroluminescence spectra	[39]
Electrodes in batteries	C(Li)	XPS	Depth profile of the solid electrolyte interface formed on the C anode in a Li battery was correlated to the extent of capacity fading	[40]
	Passive layer on Li	XPS	Observation of the layered structure and local composition of the passive film on Li formed in the presence of propylene carbonate	[41]

Table 1 (continued)

Classification	Material	DPA method(s) used	Most important aspect of DPA in the work and other remarks	Reference
	$LiNi_{0.80}Co_{0.15}Al_{0.05}O_2$	GDOES	A uniform Li depth profile was found in the lithium battery positive electrode material studied in the pristine state and after degradation	[42]
Corrosion and passive layers	Zr–50% W	GDOES, RBS	Formation of a layered ZrO_2/ZrO_2–WO_3 structure during anodization in phosphoric acid; distribution of the foreign components in the oxides and at its boundaries	[43]
	Al	GDOES	Detection of the sulfate ion migration in the passive film formed on Al with anodization	[44]
	Fe	XPS	For Fe passivation in phosphate media, subsequent oxide layers were found, and the outer layered contained P only	[45]
	Al–Mn alloy	RBS, XPS	Accumulation of manganese oxide at the surface of anodized Al–Mn samples	[46]
	Al–Ta alloys	AES, RBS	Variation of the composition and thickness of the passive layer as a function of composition and anodization conditions	[47]
	InSb	AES, RBS, EDX linescan	Formation of various types of passive layers upon anodization in sodium tungstate electrolyte	[48]
	Fe–Cr	XPS	EDTA results in a more Cr-rich surface of the passive film on the Fe–20 Cr alloy	[49]
	Sn–Ag–Cu alloys	AES, XPS	Corrosion rate decreases with increasing Ag content; Sn(II) and Sn(IV) species are formed during the corrosion while the surface becomes Ag rich	[50]
	Zn–Sn alloys	XPS	Confirmation of the electroactivity of the passivating chromate layer; identification of the components of the passive layer	[51]
	Alloys (nanocrystalline and amorphous)	XPS, AES	An extensive review on the relationship of corrosion properties and surface layer composition formed on corroding and anodized nanocrystalline and amorphous alloys	[52]
	carbon steel (SAE 1018)	XPS	Description of the depth profile of the passive layer formed with S and O in alkaline ammonium sulfide solution	[53]
	Fe/polypyrrole	GDOES	A clear bi-layer structure could be seen with DPA, showing the presence of the phos phomolybdate anion used for doping in the near-substrate polymer layer	[54]

Aim of this work

The present work aims at eliminating two crucial problems that often arise during the DPA of electrodeposited (ED) samples:

(a) Resolution loss during the DPA methods applying sputtering

When sputtering is applied to remove the actual surface layer of the specimen analyzed, not only do the bombarding ions take away the surface atomic layer(s) but secondary effects also arise. Depending on the bombarding energy, the surface atomic layers can be mixed up as a result of the impact of the colliding ions, and the sharp interfaces become distorted. In parallel with the signal convolution due to the component mixing, the actual surface roughness of the sample being sputtered can also increase, hence causing a widening of the sampling depth as referred to the original surface. For these reasons, the signal sharpness tends to decrease as the sputtering front penetrates into the sample, and

the larger the distance from the original surface, the more the composition depth profile function is smeared out. This means that the near-substrate region can be analyzed with the lowest resolution. The resolution loss with increasing sputtering depth is a common problem of the in-depth composition analysis of surface films, including all electrodeposited layers.

(b) Influence of the initial surface roughness and crater shape on the DPA results

Should a sample surface be "planar" even at the microscopic scale, the mean roughness of the surface is still much larger than the lattice plane distances, often by several orders of magnitude. If such a surface is sputtered, it is difficult to predict how the initial surface roughness changes during sputtering. The lateral inhomogeneity of the ion bombardment, which is brought about by the lateral ion energy distribution of the primary ion beam used for sputtering, can cause a serious problem by changing the ideal crater shape. In the case of insulating samples, or samples prepared on non-conductive substrates, the charge accumulation on the sample surface can change the crater shape, too. However, ED samples are mostly metallic, so this latter effect does not play a significant role in their analysis. Both high surface roughness and non-ideal crater shape make the sputtering uneven and destroy the depth resolution. There is no method to calculate the shape evolution of the sample and the sputtering-induced intermixing at the same time. If the sample contains layers and the roughness is cumulative (i.e., the relative thickness fluctuation of the layers at a particular position of the sample is the same as that of the entire sample at the same spot), the DPA will show sharp interfaces at the beginning of the sputtering and a large intermixing far from the substrate, although a cross-sectional image would tell just the opposite. The roughness-related problems can be particularly severe for ED samples, since the increase of the surface roughness of ED metals with the total thickness is much larger than for sputtered or evaporated metal coatings.

Our goal was to eliminate both above-mentioned problems by combining a technical novelty with the application of a DPA method providing high resolution and low sputtering-induced intermixing effect:

(a) The common approach of the sputtering-based DPA of essentially all sorts of sample is that the analysis starts at the final surface of the structure formed, and the sputtering crater penetrates into the sample towards the substrate. In contrast to this conventional method, we developed the reverse method. The key element of the sample preparation is the removal of the substrate from the ED sample in a gently manner so as the new surface formed has a very low mean surface roughness, and the sputtering can be started at the same interface where the ED sample started to grow. Hence, the very beginning of the electrodeposition process could be studied with a very high accuracy.

(b) Throughout this work, SNMS was used for DPA. The mild sputtering conditions used in the SNMS instrument helped to minimize both the intermixing and the sputtering-induced roughness. Another advantage of the SNMS method was that the actual composition of the surface layer of the sample can be automatically calculated without any matrix effect. Therefore, an excellent precision was achieved in the calculation of the molar fractions as a function of the deposit thickness. The change in the deposit composition with deposition time could be calculated, and the results obtained could be confronted with electrochemical data.

Below we present the results obtained for Ni-rich alloys and Co–Cu/Cu multilayers. The alloys contain Ni as the main component and Cu, Cd, Sn, Fe, and/or Co as minority components. The low concentration of the compound of the alloying element(s) in the electrolytes resulted in a significant change in the near-substrate zone, although the steady-state (or bulk) molar fraction of the alloying element was fairly low in some cases. The study of these systems proved to be technically the most feasible, but the technique presented can be applied in principle to a great variety of sample composition yet to be studied.

Experimental

Chemicals and materials

Si wafers with (100) orientation were coated by evaporation to obtain a sufficiently adherent and conductive metal layer that later served as substrate. A 5-nm-thick chromium layer was first evaporated onto the Si wafer as the adhesive layer. The subsequent conductive layer was either a 20-nm Cu layer or a 30-nm Ag layer. The latter two conductive layers proved to be equivalent in that they had no significant impact on the composition depth profiles [21]. The mean surface roughness of the metal-coated substrates was determined with an atomic force microscope (AFM) and was found to be between 1 and 3 nm [29]. Hereinafter, the notation "/" refers to the

boundary of the layers produced under the same conditions (i.e., by evaporation or by electrodeposition using the same solution), while "//" stands for separating ED layers produced using different solutions.

All chemicals used for the solution preparation were of analytical grade. Solutions were prepared with ultrapure water (ELGA Purelab, resistivity 18 MΩcm). Composition and notation of solutions used for alloy and multilayer plating will be given in the corresponding section for sake of clarity. When it was needed, zinc cover layers were deposited from the following solution: $ZnSO_4$ (0.5 mol/dm^3), H_3BO_3 (0.32 mol/dm^3), NH_4Cl (1.0 mol/dm^3), poly (vinylpyrrolidone) (3 g/dm^3), and pH=5.5. The solution for Ni plating was composed of $NiSO_4$ (0.60 mol/dm^3), Na_2SO_4 (0.20 mol/dm^3), $MgSO_4$ (0.16 mol/dm^3), NaCl (0.12 mol/dm^3), and H_3BO_3 (0.40 mol/dm^3). The solution for Ni cover layer plating was made with a technical grade Ni salt containing about 0.21% Co as impurity, and hence, the occurrence of the Co in the DPA functions indicated the interface of the layer of interest and the Ni support. The baths used for cover layer deposition were optimized so that a Ni or Zn//Ni support with a sufficiently high tensile strength and low internal stress could be obtained.

Electrodeposition

Electrodeposition was carried out in a tubular cell. The exposed surface area of the upward facing cathode was about 8 mm×20 mm, and the recessed part of the cell was 15 mm high, hence ensuring an even accessibility of the entire cathode surface. The counter electrode was a metal sheet immersed parallel to the cathode at the top of the cell. The counter electrode material varied according to the solutions used. It was mostly composed of the more noble metallic component of the electrolyte and was used as a sacrificial anode. In all experiments, a saturated calomel electrode was used as a reference, and the potential values are referred to this electrode throughout the work.

The deposition of the sample of interest was followed by either a Zn/Ni or a Ni supporting layer, where the Zn layer helped to identify the end of the Ni-rich sample during the sputtering process of the DPA. The preparation of the subsequent electrodeposited layers was performed by changing the electrolytes but without disassembling the cell. This method ensured that the same area was covered completely with the subsequent layers. The current density was −30 and −6.5 mA/cm^2 for the Zn and Ni layers, respectively. The minimum total thickness of the covering layer(s) was about 3 μm in order to achieve a sufficient toughness that enabled us to peel off the deposits from the substrate without any significant damage. Further details of the sample preparation process can be found in the earlier papers [20, 21, 27–30].

Sample preparation for the reverse depth profile analysis

After depositing the desired layer structure on the substrate, the samples together with the substrate were cut to size around their edges. Then, the back side of the Si wafer around the central region of the deposit was scratched along its crystallographic axis in order to define the breaking line. The sample was bent in a manner so that the ED layers were at the concave side; hence, they were never exposed to a tensile stress. The Si wafer was thus broken, but the deposit remained intact. Hereupon, the deposits could be detached from the Si wafer and samples with a very smooth surface were obtained. The interface along which the sample detachment could be done varied mostly as a function of the second layer of the substrate, but the deposit also had some influence. The Si/Cr/Ag substrates could be separated along the Cr/Ag interface. The separation of the Si/Cr/Cu substrates happened in most cases at the Si/Cr interface, except for the Ni–Bi samples where the weakest adherence took place at the Cu//Ni–Bi interface. When the separation took place at the Si/Cr interface, the mean surface roughness of the substrate side of the detached samples was comparable to the mean surface roughness of the Si wafer used. When the Cr layer remained at the Si wafer and Ag was the topmost layer of the detached sample, the mean surface roughness of the Ag layer increased slightly, but the composition depth profile curves were equally sharp as in the case of the Si/Cr/Cu substrate. In the resolution scale of the profilometric analysis, the Cr-terminated and Ag-terminated samples were of identical quality.

SNMS measurements and calculation of the composition depth profile functions

The (SNMS) depth profile measurements were carried out by an instrument of the type INA-X (SPECS GmbH, Berlin, Germany). The erosion in the SNMS instrument was carried out for a round-shaped area with a diameter of 2 to 3 mm defined by a Ta mask. Ar^+ ions with the energy of 350 eV were used for sputtering the samples. This ion energy is by an order of magnitude smaller than those generally used for surface layer removal in AES or XPS, and bombardment with such a low energy may lead to an intermixing of the atoms near the sample surface at a depth of at most two atomic layers. The lateral homogeneity of the ion bombardment was checked by a profilometric analysis of the depth of the craters sputtered. The sputtering rate of each layer (Cr, Cu, Ag, Co, Ni, Zn, Sn, and various Fe–Co–Ni alloys) was measured separately in preliminary experiments to establish the depth profile calculations. The method of the determination of the molar

fraction vs. depth functions was described earlier ([27] and references cited therein).

Calculations applying the DPA functions

The current efficiency of the deposition (η) was determined from the thickness of the deposits measured in the DPA experiments. It was calculated as

$$\eta = d_{SP}/d_{NOM}, \quad (1)$$

where d_{SP} is the deposit thickness as measured from the crater depth after the sputtering d_{NOM} is the nominal sample thickness as calculated from the Faraday's law by assuming the discharge of the metal cations only. The accuracy of the determination of the current efficiency was typically ±5%. When the current efficiency values obtained were scattered around one, the deviation of η from one was neglected. This was the case for the Ni–Cu, Ni–Cd, Fe–Co–Ni, and Co–Ni–Cu samples for all current densities applied.

In special cases, it is possible to relate the sputtering depth to the time passed after the start of the deposition. With this method, chronoamperometric data can be obtained for the partial current density of a particular alloy component. For this calculation, the current efficiency has to be nearly one. The partial current density of the component k (j_k) can be calculated from the composition depth profile function as the product of the local molar fraction of the component (y_k) and the total current density (j_{TOTAL}):

$$j_k = y_k\, j_{TOTAL}. \quad (2)$$

The deposition time can be calculated from the sputtering depth as follows:

$$t_{DEP} = \frac{nF}{j}\frac{\rho}{M}(d_{SP} - d_{SUB}), \quad (3)$$

where ρ is the density, M is the molar fraction, and d_{SP} and d_{SUB} refer to the sputtering depth and substrate thickness, respectively. The ρ/M ratios for several alloys studied in the present work are almost identical (like for the Ni–Cu alloys or the Fe–Co–Ni alloys with a face-centered cubic phase). Therefore, the deposition time can be easily calculated with the above linear equation, without any correction for the actual composition.

Result and discussion

DPA of ED Ni alloys

Ni–Cu alloys

Ni–Cu alloys were deposited by using two electrolytes, a solution containing chloride ions (Watts-type bath; $NiSO_4$ 0.85 mol/dm^3, $NiCl_2$ 0.15 mol/dm^3, H_3BO_3 0.4 mol/dm^3, $CuSO_4$ 3–30 mmol/dm^3, pH=2.5) and another one based on nickel sulfate and sulfamic acid ($NiSO_4$ 0.4 mol/dm^3, H_3BO_3 0.25 mol/dm^3, HSO_3NH_2 0.15 mol/dm^3, Na_2SO_4 0.3 mol/dm^3, $CuSO_4$ 10–50 mmol/dm^3, pH=3.25). Electrochemical characteristic of both electrolytes is illustrated in Fig. 3. A two-step Cu^{2+} reduction takes place in the chloride-containing electrolyte, which is indicated by the two equal current steps in the cathodic-going curves. The Cu dissolution starts at the edge of the first and second reduction steps, leading to Cu^+ as the primary dissolution product of the copper deposited. In contrast to the chloride-containing electrolyte, the transfer of the two electrons cannot be separated in the case of the sulfamate bath. Regardless of the mechanism of the Cu^{2+} reduction process, the codeposition of Cu and Ni can be classified as normal codeposition. The reduction of Ni^{2+} ions is preceded by the diffusion-limited Cu deposition regime, and the Ni codeposition starts at the same potential as in the absence of Cu^{2+} ions in the bath.

The near-substrate composition depth profiles obtained for samples deposited from the chloride electrolyte with various Cu^{2+} concentrations at −14 mA cm^{-2} current density can be seen in Fig. 4. For all these samples, the current was started within seconds after the electrochemical cell was filled up with the electrolyte. Nevertheless, all composition depth profile functions show that the Si/Cr/Cu substrate was severely damaged at the nanometer scale. As the Cu^{2+} concentration increased, the maximum molar fraction of both Cr and Cu decreased, and the Cr signal became finally undetectable for $c(Cu^{2+})$=30 mM. The reason of the substrate damage is the synproportionation reaction ($Cu+Cu^{2+}+8\ Cl^-=2\ [CuCl_4]^+$) and the oxidation of chromium by the Cu^{2+} ion ($2Cu^{2+}+Cr+8\ Cl^-=Cr^{2+}+2[CuCl_4]^+$; oxidation to Cr^{3+} is also possible). These reactions are undetectable at the macroscopic scale during the short time between the filling up of the cell and the start of the current, and the metallic coating of the substrate remaining on the Si surface exhibits a large enough conductivity to obtain a deposit in which the pinholes of the metallic coating of the substrate can no longer be seen. Nevertheless, the corrosion processes left behind a damaged substrate where the even layer structure and the sharp interfaces could no longer be taken advantage of.

The corrosion of the substrate was much less severe for the electrolyte that contained no chloride ions. Figure 5 shows a typical composition depth profile curve obtained with the sulfamate bath. The initial Cr layer is intact, and the subsequent Cu layer is also quite sharp. A little Ni appears when the Cr layer is finished, indicating the pinholes formed in the Cu layer, but the oxidation of Cr was insignificant in the absence of the chloride ions. It is thought that the top Cu layer of the Si/Cr/Cu substrate was

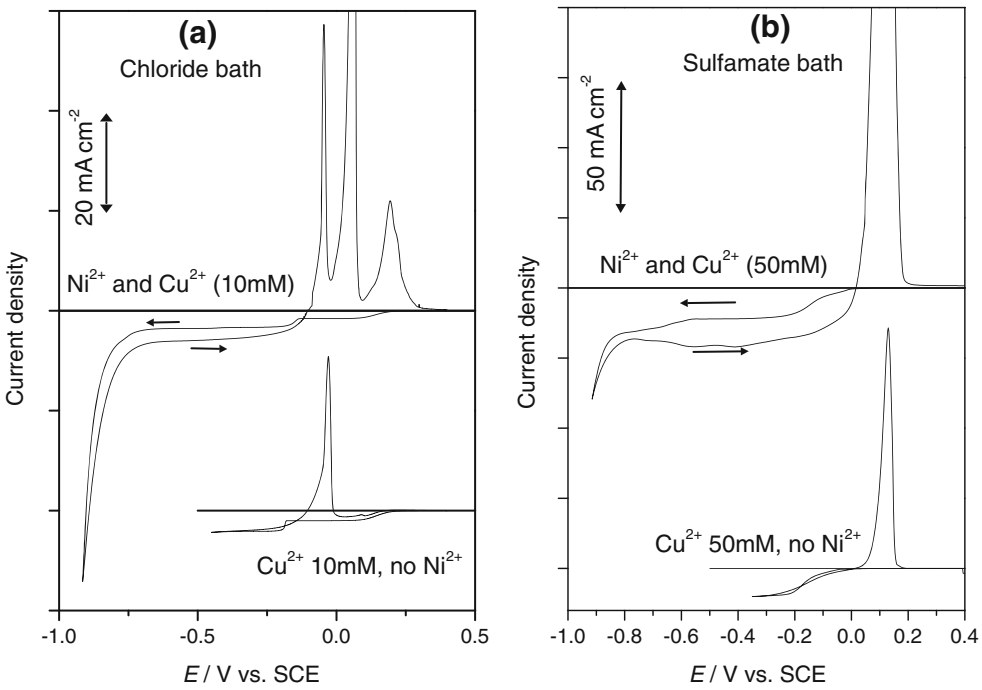

Fig. 3 Polarization behavior of the Ni–Cu system as measured on a Pt microelectrode at 5 mV/s sweep rate. **a** Chloride bath, **b** sulfamate bath

also reconstructed a bit due to the Ostwald ripening of the small Cu crystals of the substrate due to the exchange current with the Cu^{2+} ions of the electrolyte. This process may also roughen the substrate surface, but this process was much less significant than the corrosion in the presence of the chloride ions.

The inset of Fig. 5 also presents how the Co impurity of the Ni cover layer was applied to detect the interface of the first and second deposits even in the case when both contain nickel. As the Cu content of the sample sputtered decreases, the molar fraction of the Co increases. This region of the sample can be used to estimate the sample thickness and hence to assess the current efficiency during the deposition. The width of this interface is also indicative of the final roughness of the deposit layer. Since the roughness of the deposit is much larger than the sputtering-induced roughness at the same thickness scale, the widening of the transition zone between the Ni–Cu alloy and the Ni(Co) top layer can be solely attributed to the impact of the deposit roughness.

The deposits prepared were designed to exhibit 10–15 at. % Cu in the bulk deposit. The preliminary calculation was based on the diffusion-limited Cu deposition current density as measured at a potential where no Ni codeposition can

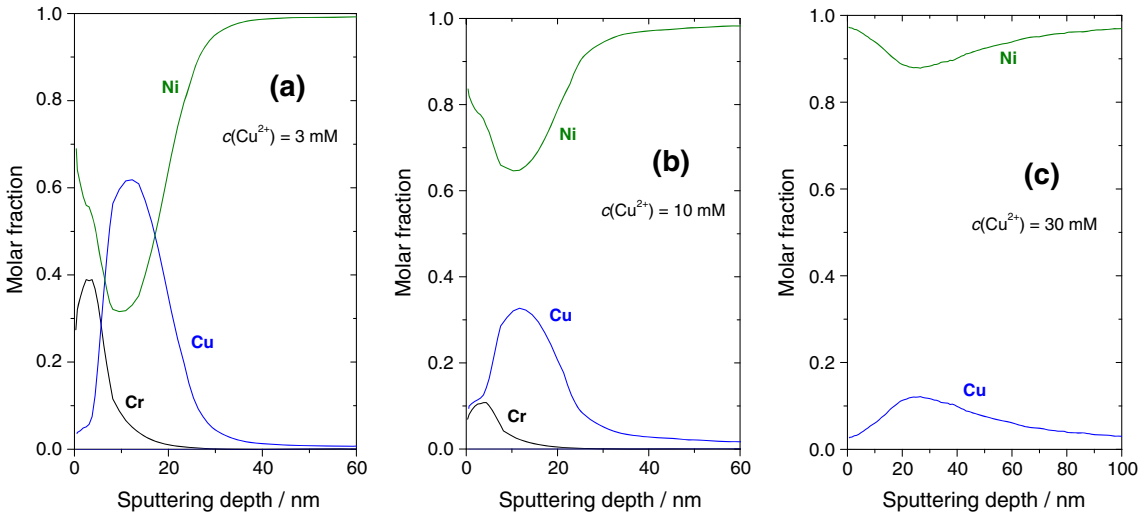

Fig. 4 Near-substrate reverse composition depth profile of ED Ni–Cu samples obtained from the chloride baths of various Cu^{2+} concentrations at -14 mA cm^{-2} current density

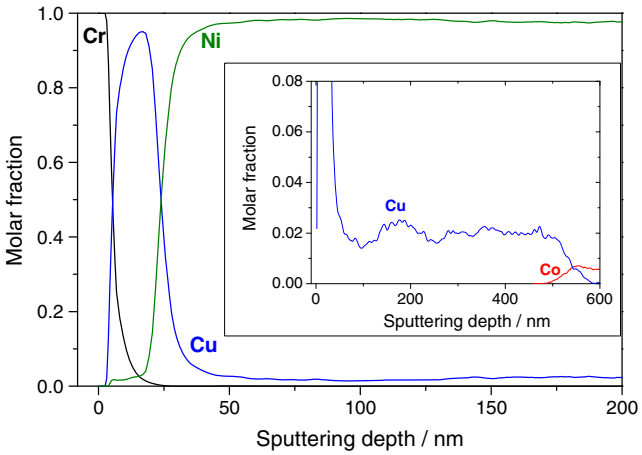

Fig. 5 Near-substrate reverse composition depth profile of an ED Ni–Cu samples obtained from the sulfamate baths with 15 mM Cu^{2+} concentrations at −12 mA cm^{-2} current density. The *inset* shows the magnified Cu and Co composition depth profile throughout the entire sample

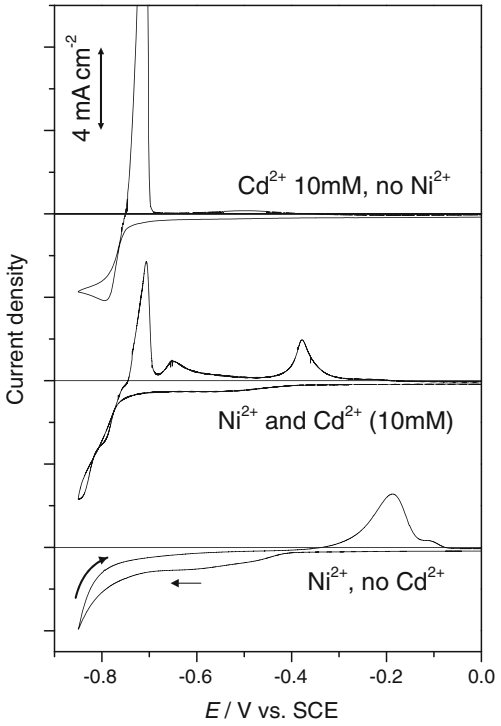

Fig. 6 Polarization curves obtained for the deposition of Cd, Ni, and Cd–Ni alloy on a Pt microelectrode at 5 mV/s sweep rate

take place. Regardless of the bath type used, the experience was that the actual Cu partial current density (as calculated with Eq. 2) was much less that that inferred from the experiments when only Cu was deposited (i.e., from conventional chronoamperometric curves). This experience verifies the approach introduced by Kazeminezhad et al. [55] for the electrochemical alloy preparation by a two-pulse-plating method, depositing a sub-monolayer portion of the corresponding alloying element in one of the subsequent pulses. This method called "precision plating" by the researchers introducing it proved to be easy to design the composition of Ni–Cu alloys, and the physical properties of the resulting deposit evidenced a good homogeneity at the atomic scale [56–58]. It is clear from the DPA functions of the d.c. plated Ni–Cu alloys that neither the composition design nor the homogeneity can be achieved with d.c. plating.

Ni–Cd alloys

Ni–Cd alloys were deposited form a similar chloride-containing electrolyte that was used for obtaining one group of Ni–Cu samples, except for that $CdSO_4$ (10 or 30 mmol/dm^3) was used instead of $CdSO_4$. For experiments to study the deposition of Cd alone, $NiSO_4$ was replaced with $MgSO_4$.

The polarization behavior of the Ni–Cd system is shown in Fig. 6. The deposition potential of Cd is −0.75 V, and the Ni onset of the deposition took place at −0.79 V. Due to the low Cd^{2+} concentration, the Ni codeposition starts approximately at the same potential where the Cd deposition becomes mass transport limited. In the presence of Ni^{2+}, the charge balance indicates that the cathodic current in the forward curve at potentials more positive than −0.79 V cannot lead to a metal deposition but it accounts for hydrogen evolution. When the cathodic limit of the sweep was −0.79 V for the electrolyte void of Cd^{2+}, the stripping peak disappeared.

The standard potential of Ni^{2+}/Ni couple is 170 mV more positive than the standard potential of the Cd^{2+}/Cd couple (data refer to systems without any complexing agent; standard potentials for chloride solutions are not available). Nevertheless, the deposition of Cd occurs at more positive potentials than Ni. Therefore, Cd behaves as a metal of higher deposition preference, although it is less noble in the thermodynamic sense.

It is expected that the little difference in the deposition potential of Cd and Ni makes the system prone to the formation of Ni–Cd alloys. This assumption is supported by the appearance of two new stripping peaks for the dissolution of the Cd–Ni deposit at −0.64 and −0.38 V. These peaks correspond to the Cd_5Ni and CdNi alloys, respectively [59]. In contrast to Ni–Cd sulfate baths without chloride ions [60], the presence of Cd^{2+} does not suppress the deposition of Ni. While the deposition of pure Cd could not be seen in the polarization curves of the chloride-free solutions [60], it was clearly observed in our polarization data.

It is expected from the deposition potentials of Cd and Ni that the deposition of a Ni–Cd alloy will start with a Cd-rich zone. Figure 7 shows the composition depth profile of

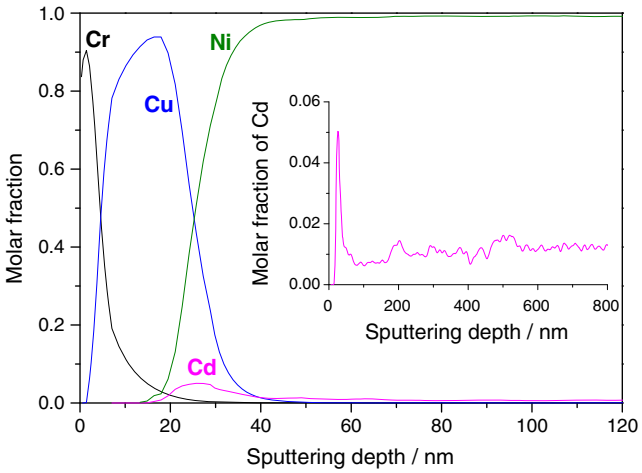

Fig. 7 Reverse composition depth profile curve measured for a Ni–Cd sample deposited at −19.5 mA cm^{-2} from an electrolyte with 10 mM Cd^{2+} concentration

a sample deposited with −19.5 mA cm^{-2} current density from an electrolyte containing 10 mmol/dm^3 Cd^{2+}. The composition depth profile data of the Ni–Cd deposits support the assumption that a Cd-enriched zone must exist in the near-substrate region. However, the Cd molar fraction of the deposit near the substrate seldom reaches a value larger than 0.05 or 0.12 for $c(Cd^{2+})$=10 and 30 mM, respectively. This indicates that although Cd has the less negative deposition potential in the Ni–Cd metal pair, the deposition or the nucleation of Cd is very hindered. As the deposit grows, the Cd molar fraction reaches a minimum after a fast decay, and then a little increase of the Cd content can be seen (see the inset of Fig. 7). The minimum occurs after the deposition of a 70–90-nm-thick layer, depending on the concentration and the current density. This minimum in the molar fraction of the preferentially deposited metal after the nucleation zone can be seen for many systems (see also the alloys discussed in "Fe–Co–Ni alloys"–"Co–Ni–Cu alloys" sections) and yet to be explained. The Cd molar fraction in the bulk deposit was around 0.02 and 0.06 for $c(Cd^{2+})$=10 and 30 mM, respectively. The partial current density of the Cd deposition during the Ni–Cd codeposition was 40% to 50% of steady-state current density for the deposition of Cd from a Ni-free solution. Therefore, a much higher Cd concentration was expected in the Ni–Cd deposits. These data show that the codeposition of Cd besides Ni is hindered when the Cd concentration is low.

The observation of the Ni–Cd//Ni interface in the composition depth profile functions indicates that the Ni–Cd samples could be deposited at a high current efficiency (see Eq. 1). The deposit thickness as measured by DPA was in agreement with that calculated from the deposition parameters with Faraday's law. In this respect, there is no difference between the sulfate [61] and chloride-sulfate Ni–Cd solutions (present work).

Ni–Sn alloys

Ni–Sn alloys were deposited form an electrolyte with identical $NiSO_4$, $NiCl_2$, and H_3BO_3 concentrations to those in the chloride containing Ni–Cu solution. However, the pH had to be set to 1 in order to suppress the hydrolysis of the Sn^{2+} cations. The $SnCl_2$ concentration was 3 or 10 mmol/dm^3. The onset of the electrodeposition of Sn can be seen at −0.5 V (see Fig. 8); therefore, the difference of the deposition potentials of the alloying elements is significantly larger in the Ni–Sn system than for the Ni–Cd pair. In this respect, the Ni–Sn pair is similar to the Ni–Cu pair where the diffusion-limited deposition of the more noble element takes place in a wide potential rage prior to the alloy formation. Additionally, no Ni codeposition starts at −0.79 V, but the Ni deposition is hindered on the Sn-covered electrode surface.

The reverse depth profile curve obtained for 3 mM Sn^{2+} concentration at −15 mA cm^{-2} current density (see Fig. 9) shows that there is a little Sn accumulation at the substrate side of the deposit, as it is expected from the higher nobility of Sn. The initial Sn molar fraction is as low as 0.03, and it decays fast, achieving a minimum in Sn molar fraction after an approximately 50-nm-thick deposit. The total deposit thickness in the Ni–Sn system was always much smaller than expected from Faraday's law, likely due to the low pH of the electrolyte which promotes the evolution of hydrogen. The current efficiency for the 3-mM Sn^{2+} solution was about 18%. Despite the stirring effect of the hydrogen evolved, the Sn partial current density during the deposition was much smaller than the steady-state Sn deposition at potentials where Ni codeposition is not possible. The exclusion of Sn is probably due to both kinetic and thermodynamic reasons. The lack of a stable Ni–Sn phase with low Sn content may play a role in the

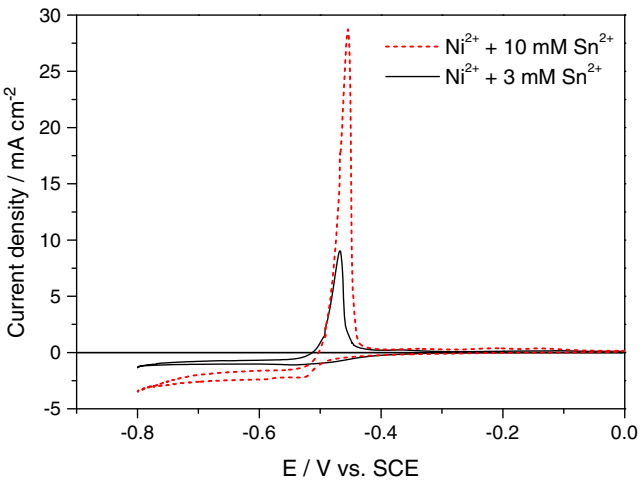

Fig. 8 Polarization curves obtained for the deposition of Sn from Ni–Sn electrolytes of various Sn^{2+} concentrations at 5 mV/s sweep rate

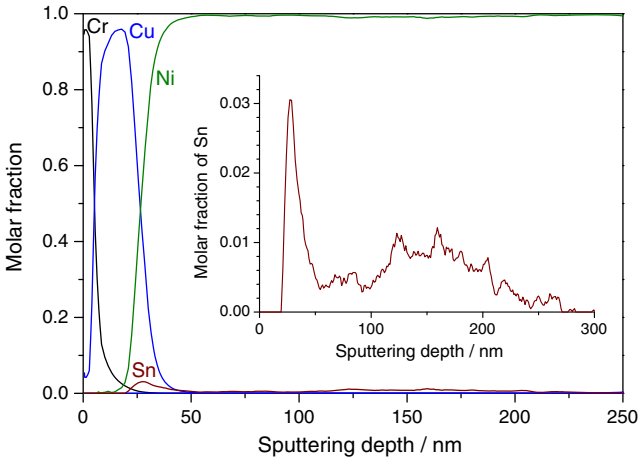

Fig. 9 Reverse composition depth profile curve measured for a Ni–Sn sample deposited at −15 mA cm^{-2} from an electrolyte with 3 mM Sn^{2+} concentration

suppression of the Sn codeposition (Ni_3Sn has the lowest Sn content among the stable Ni–Sn phases [59]).

When the Sn^{2+} concentration was increased to 10 mM, the character of the depth profile functions became fundamentally different. The initial Sn content of the deposit was often larger than 0.9 at the beginning of the sputtering. In the reverse composition depth profile obtained for a sample deposited from 10 mM Sn^{2+} electrolyte (Fig. 10a), an inflection can be seen in the Sn molar fraction at about an 80-nm distance from the initial surface. Then, the Sn signal decreases in an approximately linear manner between 100 and 200 nm. This decrease is due to the onset of the dendritic growth on an initially compact deposit. From the end of the plateau between 50 and 80 nm, the Ni–Sn deposit and the Ni cover layer overlap. This overlap can also be detected very well by measuring the impurities (especially Co) in the two layers. The current efficiency in this case was about 14%. For the calculation of the current efficiency, the thickness was measured where both the Sn signal decreases and the Co signal increases to the half of its maximum value, and this distance was taken as the mean sample thickness.

Interestingly, the high initial Sn content was accompanied in all measurements with the disappearance of the substrate layers. Some trace amount of Cr could be detected in the close vicinity of the surface of the detached sample (see Fig. 10a, bottom part), but the initial molar fraction of Cr was as low as 6×10^{-4}, as opposed to nearly 1 observed for many other samples. The Cr signal fell fast and reached the natural background level of less than 15 counts/s within a 20-nm sputtering depth. While no Cu was found on the surface of the detached Si wafer, the Cu signal extended very much to the bulk of the deposit. One can exclude that the lack of the substrate layer was due to the damage of the sample surface during the peeling-off procedure, since in this case not only the Cr signal but also the Cu signal should be absent. It is also unlikely that the substrate layers peeled off during the deposition, since this would lead to a complete destruction of the substrate and of the deposit. If these were true, the Cr signal intensity should be proportional to that of the Cu. However, Cr was practically absent, while Cu was detected at all depths where the Ni–Sn deposit was seen.

Figure 10b shows the intensity vs. depth curve for a Ni–Sn sample. It is the common character for samples deposited with 10 mM or higher Sn^{2+} concentration that on the logarithmic scale, the Sn and Cu intensities make parallel functions. Therefore, the Cu concentration is

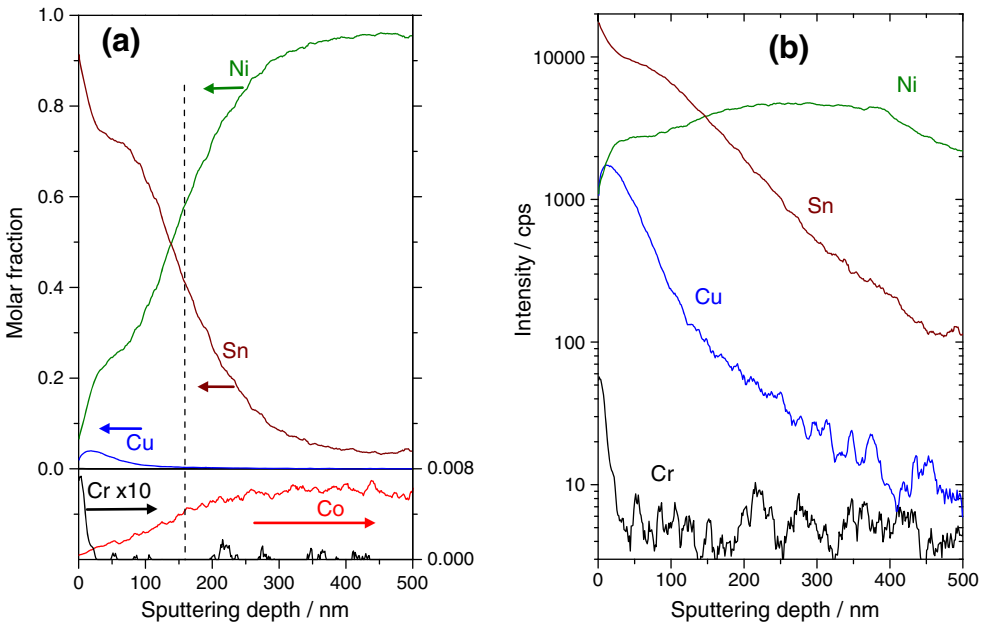

Fig. 10 **a** Reverse composition depth profile curve measured for a Ni–Sn sample deposited at −15 mA cm^{-2} from an electrolyte with 10 mM Sn^{2+} concentration. The *dashed line* shows the mean sample thickness. **b** The intensity vs. sputtering depth curve of the same measurement

proportional to the Sn concentration in the deposit. The only origin of Cu in the deposit is the substrate. The integration of the Cu signal along the entire sample cross section revealed that the amount of Cu was never larger than the quantity of Cu in the substrate layer. The electrolyte with 3 mM Sn^{2+} concentration was prepared from the same stock solution, and the Cu intensity vs. sputtering depth function in this case was conformal to the nominal structure of the substrate. The same applies for samples containing alloying elements other than Sn. The Ni cover layer was always void of any Cu impurity.

The migration of Cu within an electrodeposited alloy layer or onto the top of an electrodeposited layer has been known for Ni–Fe [17] and Ni–Fe–Cr–Mo deposits [18]. In the case of the Ni–Fe alloys [17, 18], the migration of Cu led both to the contamination of the electrodeposited alloys with Cu and to the accumulation of a Cu layer on the electrolyte side of the deposit. In the present study, the amount of Cu in the substrate was definitely too small to form another Cu layer at the electrolyte side of the Ni–Sn deposit. However, the alloying of the Sn-rich deposit with Cu via the migration of the Cu atoms originating from the substrate layer was confirmed. Our preliminary DPA results show that Ni–Bi samples have a similar behavior than the Ni–Sn samples in the sense that the substrate Cu layer tend to diffuse into the deposit.

Fe–Co–Ni alloys

Fe–Co–Ni alloys were deposited by using electrolytes with the following composition: $NiSO_4$ (0.2 mol/dm^3), $CoSO_4$ (8 to 75 mmol/dm^3), $FeSO_4$ (8 to 25 mmol/dm^3), and H_3BO_3 (0.4 mol/dm^3), pH=2.8. The reverse composition depth profile functions for two samples deposited with identical current density but different Fe^{2+} and Co^{2+} concentrations are shown in Fig. 11. All reverse depth profile functions were very sharp in the near-substrate zone. Both the Cr and the Cu layers could be identified clearly, and their thickness was in agreement with the nominal 5 and 20 nm, respectively. No Cu migration was detected (c.f. Ni–Sn alloys). The good resolution of the reverse depth profile analysis is demonstrated by the fact that the Cu molar fraction reaches 1, even though the layer thickness is as small as 20 nm. The interface between the evaporated metal layers and the deposit was sharp and undistorted. Therefore, the corrosion of the Cu substrate layer by the electrolyte could be excluded.

The near-substrate zone (up to about 150 nm) of all depth profile functions measured followed the same pattern. Namely, the Fe–Co–Ni deposits were initially very rich in Fe, following the deposition preference characteristic for the anomalous codeposition. Since the concentration of the Fe^{2+} ions was relatively small in the bath, the electrolyte

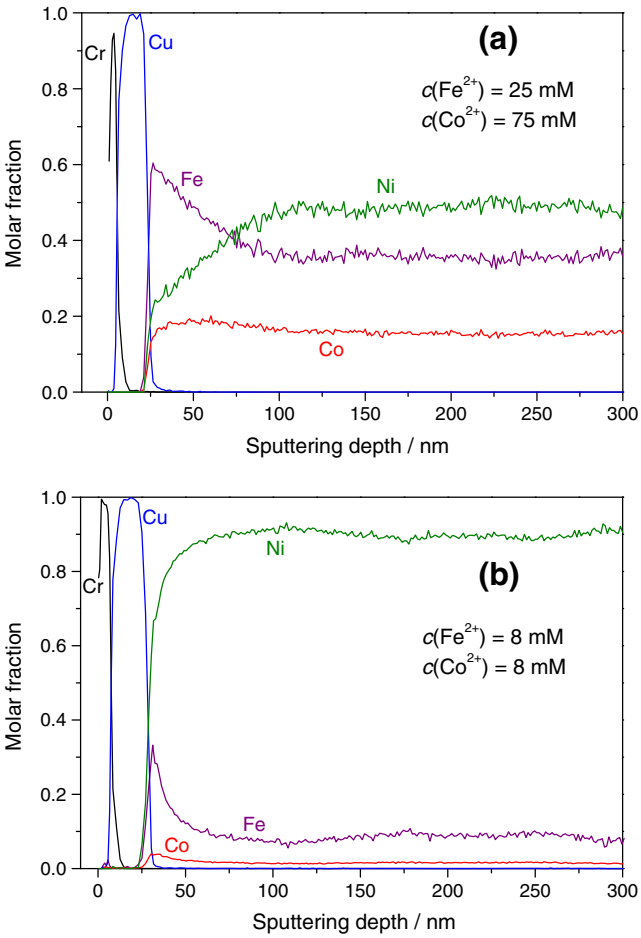

Fig. 11 Reverse composition depth profile curves of Si/Cr(20 nm)/Cu(20 nm)//Fe–Co–Ni samples deposited at −12 mA cm^{-2} from electrolytes of various Fe^{2+} and Co^{2+} concentrations

depletion in the vicinity of the cathode took place fast, and the Fe molar ratio in the deposit immediately started to fall. The decrease in the reduction rate of Fe^{2+} ions had to be compensated by the discharge of other ions because the current was constant. The molar fraction of Co in the deposit increased slightly at the beginning, and it reached a maximum soon after the start of the deposition (within about 40 nm deposit thickness). In this region, the changes of the molar fraction of Fe and Co are uncorrelated. The Ni molar fraction kept increasing throughout the near-substrate zone, and it reached a maximum at the last among the three alloying elements. The distance at which the molar fraction of a particular component reached the maximum was the smaller, the higher the deposition preference of the metal.

The high deposition preference of iron is demonstrated by the composition depth profile data for the sample where the concentration of Fe^{2+} and Co^{2+} were the same in the electrolyte (Fig. 11b). Although the deposition of both Fe and Co is preferred as compared to the deposition of Ni, the Fe molar fraction was much larger than the Co molar fraction in both the initial and in the steady-state zone.

A great advantage of the DPA over the measurement of the average composition is that the local correlation of the molar fractions can be revealed. Figure 12 presents the molar fraction of Co and Ni as a function of the molar fraction of Fe for the sample deposited under the following conditions: j=−16 mA cm^{-2}, c(Fe^{2+})=25 mmol/dm^3, and c(Co^{2+})=75 mmol/dm^3. In the cases when the deposit composition showed some fluctuation even beyond the nucleation zone (see the inset of Fig. 12 for the corresponding DPA function), it could be established that the molar fraction of Co is linearly proportional to the molar fraction of Fe. The observation of the local correlation of the molar fractions is a novelty, which deserves further explanation.

In the electrolyte, the Co^{2+} concentration was three times of the Fe^{2+} concentration. However, the Co molar fraction in the deposit was about 0.35 times of the Fe molar fraction. If the reduction of the Fe^{2+} ions is mass transport limited, the maximum available partial current density for the Co deposition should also be about three times of the Fe partial current density. This assumption stems from the fact that the diffusivity of the ions of same charge, of same aquacomplex, and of almost identical molar weight should be of about the same value, and hence, the diffusion-limited partial currents must be proportional to the ion concentrations. Instead of the 3:1 cobalt–iron ratio in the deposit, the value found was nearly 1:3, indicating that the Co deposition was not mass transport limited. Since the Co molar fraction in the deposit was strictly proportional to the Fe molar fraction, one can assume that the Co^{2+} reduction rate was kinetically regulated by the iron deposition rate. At the same time, the Ni deposition rate was always as large as needed to account for the current not corresponding to the deposition rate of Fe and Co. Such extra kinetic information cannot be derived from overall composition data.

Earlier results for the composition depth profile of Fe–Co–Ni alloys were controversial [62–65], and the change in the average composition with the total deposit thickness has not been explained. It was the reverse depth profiling method that made it possible to obtain reproducible data that could be elucidated in terms of the anomalous codeposition and electrolyte depletion near the cathode. Further details of the DPA of Fe–Co–Ni alloys can be found in our earlier publications [20, 21].

Figure 13 presents the comparison of the partial current for the Fe^{2+} reduction during the deposition (curve a) and the reaction rate of the Fe^{2+} ion when no deposition took place (curve b). The diffusion-limited Fe deposition could not be measured with a blank electrolyte without Ni^{2+} and Co^{2+} ions because of the large hydrogen evolution rate at potential where the Fe deposition process becomes diffusion limited. Therefore, the mass transport limitation was carried out by studying the Fe^{2+} oxidation on an inert electrode, and the data were corrected by taking into account the number of electrons involved in each reaction.

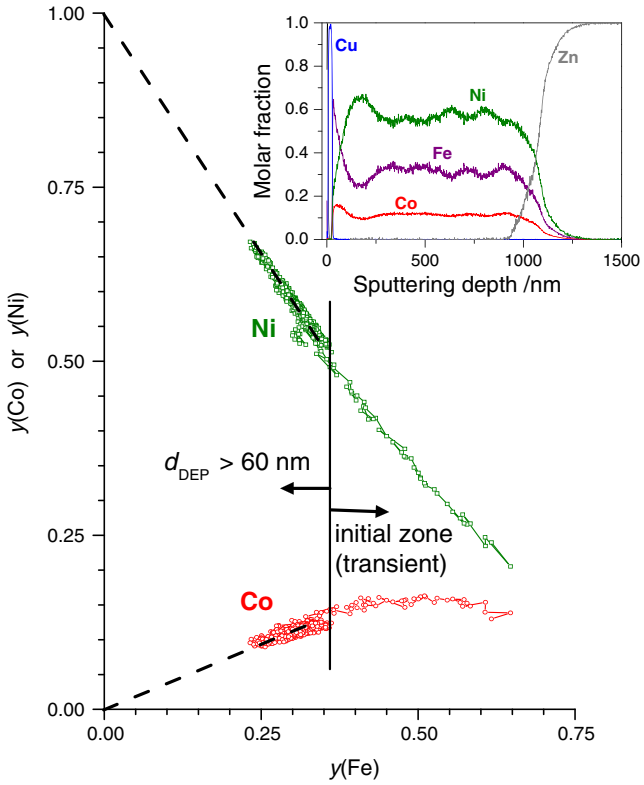

Fig. 12 Molar fraction of Co and Ni as displayed as a function of the molar fraction of Fe for a sample deposited at −16 mA cm^{-2} from an electrolyte with c(Fe^{2+})=25 mM and c(Co^{2+})=75 mM. The *inset* shows the full reverse composition depth profile function of the same sample, including the Zn cover layer

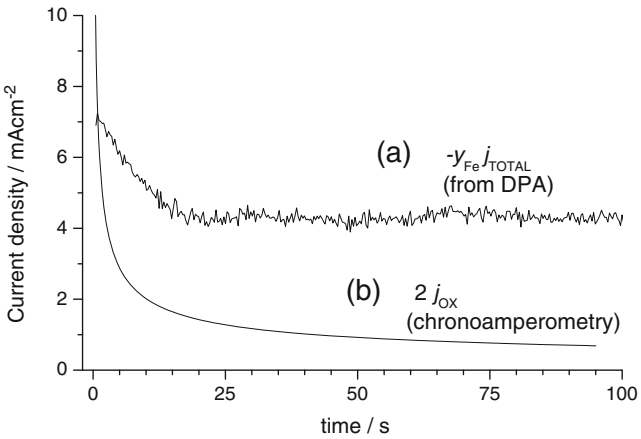

Fig. 13 Comparison of the partial current of the Fe^{2+}-related reactions. **a** Chronoamperometric curve obtained from the SNMS depth profile function for the Fe^{2+}+2e=Fe reaction for the same sample as shown in Fig. 11a. **b** Conventional chronoamperometric curve measured with a Pt electrode for the Fe^{2+}=Fe^{3+}+e reaction (the current density is doubled for the sake of a correct comparison with the two-electron deposition process)

Figure 13 shows that the relationship of the partial currents observed in situ during the alloy deposition and ex situ is the opposite than the trend fond for Ni–Cu and Ni–Cd alloys. For the Fe–Co–Ni alloys, the partial current density for Fe^{2+} reduction during the deposition process is larger than expected from the chronoamperometric behavior of the same ion. This is yet to be explained. One can speculate that the hydrogen evolution taking place during the alloy deposition as a side reaction may have some convective effect. Nevertheless, the hydrogen evolution rate could not be determined from the depth profile curves since accuracy of the estimation of the current efficiency was about 5% only. Within this error level, the deposit thickness measured during the sputtering was in accord with the nominal one. The demonstration of the hydrogen-induced convection requires the determination of the hydrogen evolution rate with an order of magnitude better accuracy.

Co–Ni alloys

Co–Ni samples were deposited essentially from the same solution as the Fe–Co–Ni samples, but $FeSO_4$ was omitted and $CoSO_4$ was applied in the same concentration as $FeSO_4$ in the ternary bath for the sake of the comparison ($c(Co^{2+})$=25 mmol/dm^3). A reverse depth profile function is shown in Fig. 14. The figure shows a sample obtained with −12 mA cm^{-2}, and the composition depth profile curves were similar when −16 or −20 mA cm^{-2} current density was applied.

Comparing to the depth profile function shown in Fig. 11a, it can be seen that the initial Co molar fraction in the Co–Ni deposit is only 0.14, while the initial Fe molar fraction was between 0.6 and 0.7 in the Fe–Co–Ni samples

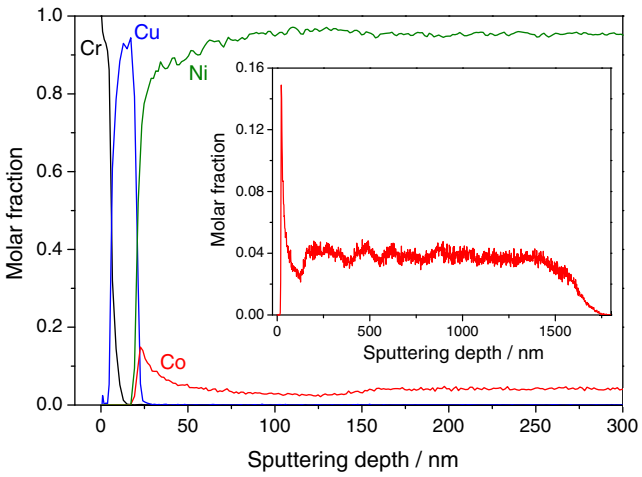

Fig. 14 Reverse composition depth profile curve of Si/Cr(20 nm)/Cu(20 nm)//Co–Ni sample deposited at −12 mA cm^{-2}. Co^{2+} concentration: 25 mM (same as $c(Fe^{2+})$) for the curve in Fig. 11a). The *inset* shows the molar fraction of the cobalt as a function of the sputtering depth for the entire sample with higher resolution/

obtained under similar conditions (i.e., same current density and same concentration of the ions of the metal with the higher deposition preference). This clearly indicates that the deposition preference of Co besides Ni is weaker than that of Fe. The maximum in the Co molar fraction occurs in the close vicinity of the substrate. In this sense, Co plays the same role in the Co–Ni alloys as Fe in the Fe–Co–Ni alloys, i.e., it is the metal with the highest deposition preference. The results obtained for the Co–Ni samples indicate that the occurrence of the Co maximum at about 40-nm deposit thickness in the Fe–Co–Ni samples is the interplay of three factors, namely the deposition preference of Co besides Ni, the decrease of the Fe molar fraction in the deposit, and the depletion of the electrolyte for Co^{2+} ions.

The minimum of the molar fraction on the preferentially deposited metal (here, Co) can be clearly seen in the inset of Fig. 14. The thickness of the initial zone was of the same order of magnitude (150 nm) as for other sample compositions.

Co–Ni–Cu alloys

The Co–Ni–Cu samples are related to the Fe–Co–Ni samples in the sense that in both alloy types there are two metals whose deposition is preferred. The electrolyte for Co–Ni–Cu deposition was the same as that used in the Co–Ni sample preparation ($c(Ni^{2+})$=0.2 mol/dm^3, $c(Co^{2+})$=25 mmol/dm^3, and $c(H_3BO_3)$=0.4 mol/dm^3) except for the $CuSO_4$ that was added in 10 mmol/dm^3 concentration. The samples were made by using Si/Cr (5 nm)/Ag(30 nm) substrates in order to detect the variation of the Cu signal with no interference with the Cu content of the topmost substrate layer.

No Cr signal was detected in the reverse depth profile curves because the Cr layer remained on the Si wafer when the deposit was detached. Although the Ag layer thickness that remained on the deposit was about one quarter of the nominal layer thickness, the signals of the elements of the deposit were equally sharp as for the Si/Cr/Cu substrates, and no signal convolution due to the sample roughening was seen in the composition depth profile curves.

The depth profile function curve in Fig. 15 shows that both Cu and Co have a molar fraction maximum near the substrate. In all Co–Ni–Cu samples analyzed, the Cu maximum occurs at the substrate/deposit interface. Cobalt starts incorporating into the sample only when the deposit thickness achieves at least 1 nm, and hence, the maximum of the Co molar fraction occurs at about 4-nm deposit thickness.

Since Cu is the most noble metal in the Co–Ni–Cu alloy and it is deposited with the normal codeposition mode with Ni^{2+}, Co^{2+}, and even in the presence of both, it is expected that as long as the Cu transport rate makes it possible, a pure Cu layer should be formed at the beginning of the

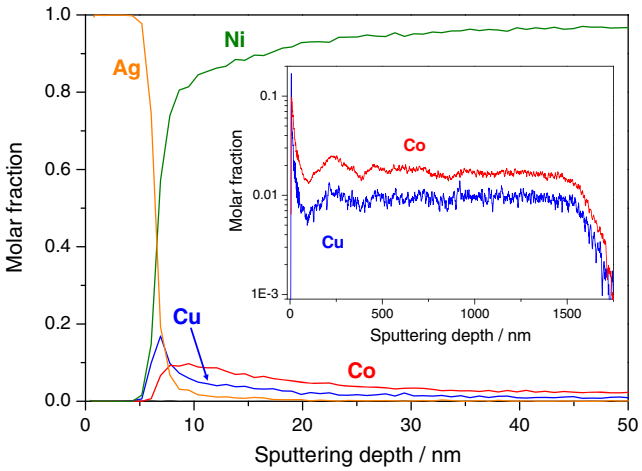

Fig. 15 Near-substrate reverse composition depth profile function of a Ni–Co–Cu sample deposited at −20 mA cm^{-2} (*main figure*) and the magnification of the Co and Cu molar fractions in the entire sample (*inset*)

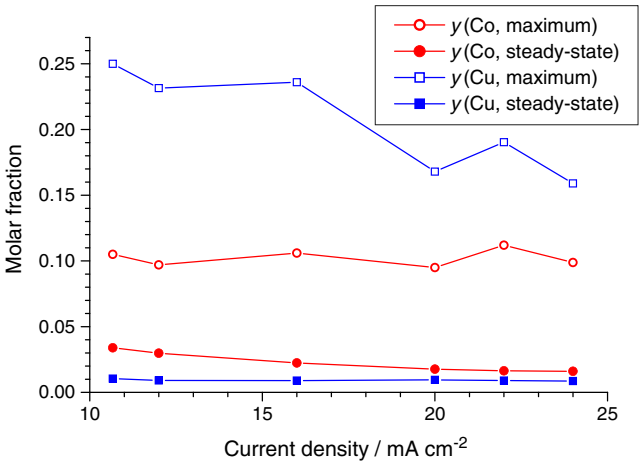

Fig. 16 Characteristic distances describing the composition depth profile functions of Cu and Co within the Ni–Co–Cu samples as a function of the deposition current density

deposition. However, we cannot see a pure initial Cu layer in the DPA results. As it can be seen in Fig. 15, the Ag substrate layer is followed with an alloy in which the initial molar fraction of Cu is about 0.18, i.e., much lower than one. This can be explained with two main reasons: (a) The time interval while the Cu^{2+} transport rate is high enough to maintain the current density applied, the number of atomic layers deposited is less than four. The thickness of such a thin layer is smaller than the in-depth resolution of the SNMS analysis. Therefore, the convolution of the real depth profile function with the depth resolution function smears out the signal measured. (b) Even if the Cu^{2+} transport rate is high enough to result in the deposition of pure Cu at the beginning of the deposition, the Cu atoms produced do not surely form a layer, but a Volmer–Weber type growth is also possible. The uneven lateral distribution of the initially deposited Cu atoms may leave a part of the Ag substrate surface uncovered that can be later occupied by Ni or Co atoms. Therefore, the molar fraction of Cu can be smaller than 1 due to the nucleation mode if a layer-by-layer deposition cannot take place.

Figure 16 summarizes the characteristic molar fractions of Co and Cu. The maximum (or initial) molar fraction of Cu decreases with the increase in the current density. This trend indicates that the decrease in the Cu molar fraction is related to the mass transport control of the Cu deposition. Simply speaking, the higher the current density, the larger the amount of Ni and Co codepositing with Cu already in the near-substrate zone, and the Cu deposition rate cannot increase to a value larger than that determined by the Cu^{2+} ion transport rate in this phase of the deposition. However, the steady-state Cu molar fraction was independent of the total current density, and the partial current density of the Cu deposition is smaller than the Cu deposition rate when Cu is deposited alone. The explanation for the unexpectedly low partial current density of Cu deposition is again the inhibition of the Cu codeposition besides Ni, similarly to the Ni–Cu alloys ("Ni–Cu alloys" section).

The Co molar fraction shows a completely opposite trend than the Cu molar fraction. The maximum of the Co molar fraction near the substrate/deposit interface is independent of the current density, but the steady-state Co molar fraction decreases with increasing current density. The reason for the difference in the behavior of Cu and Co may be sought in the different codeposition modes of these metals with Ni (normal codeposition of Cu and anomalous codeposition of Co). The detailed explanation would require a complicated kinetic simulation, which is much beyond the scope of the present work. However, any kinetic model to be applied has to be able to reproduce the present results.

Figure 17 shows the correlation of the molar fraction of the deposit components. The correlation between the molar fractions of Cu and Co can be clearly established. Similarly to the Fe–Co–Ni alloys, the deposition rate of Ni is as large as needed to pass the current not involved in the discharge of the two metals of higher deposition preference. It can be seen that, regardless of the nature of the codeposition process, there occurs a correlation between the molar fractions of the preferentially deposited alloy components.

Discussion of the DPA of the alloys studied

It has been shown for a variety of electrodeposited alloys that the preferentially deposited metal is accumulated in the near-substrate zone. This initial zone was found to be about 150 nm thick for the Ni alloys deposited at room temperature. Although this initial accumulation effect is often neglected when the deposit thickness is several micrometers, it may have various consequences:

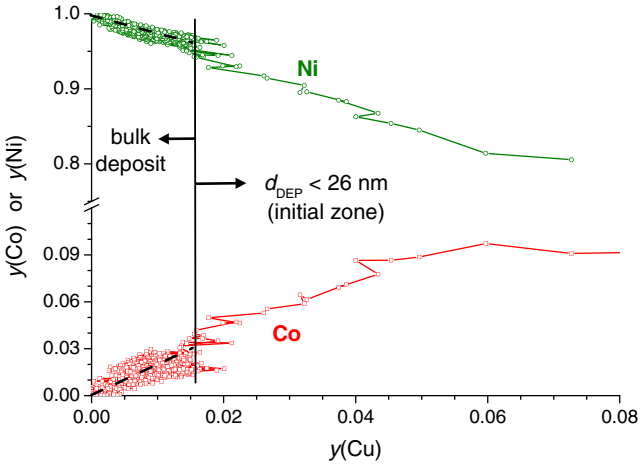

Fig. 17 Molar fraction of Co and Ni as displayed as a function of the molar fraction of Cu for a Ni–Co–Cu sample. The corresponding composition depth profile function can be seen in Fig. 15

1. Thin film technology nowadays often requires ultrathin layers. When the desired deposit thickness becomes comparable to the thickness of the initial zone, the alloy coating produced by electrodeposition can no longer be taken as homogeneous.
2. The adherence to the substrate surface is determined by the first few atomic layers deposited. Therefore, the bulk composition of the deposit cannot be used for the assessment of the adherence, but the initial deposit composition has to be known. The transition zone between the substrate and the bulk deposit was about 150 nm for the alloys studied in this work. These pieces of information have to be taken into account in the coating design.
3. The uneven deposit composition may lead to a stress in the near-substrate zone. Apart from obvious mechanical consequences, thin magnetic deposits may exhibit very different magnetic properties than the bulk alloys. Although the saturation magnetization would level off at the length scale of the initial composition modulation, the internal stress can significantly increase the coercivity via the magnetostriction of the alloy. Hence, it is very important to be aware of the nature of the composition changes in the initial zone. A prominent example is the Fe–Co–Ni alloy group discussed above.

From the viewpoint of electrochemistry, particularly interesting are the DPA measurements when two preferentially deposited components were present in a minor concentration besides the main component of the deposit (Fe and Co in Fe–Co–Ni alloys; Cu and Co in Co–Ni–Cu alloys). In both cases, the metal of the highest deposition preference accumulated at the substrate/deposit interface. As the molar fraction of the metal with the highest deposition preference started to decrease due to the electrolyte depletion in the vicinity of the cathode, the molar fraction of the next metal in the row of preference also achieved a maximum. This pattern of the evolution of the sample composition was independent of the codeposition mode.

After the nucleation zone, the molar fractions of the preferentially deposited metals show a strong correlation. This correlation was verified for both the Fe–Co–Ni and the Co–Ni–Cu deposits. In the Fe–Co–Ni system, the Co incorporation rate was regulated by the maximum Fe incorporation rate. Hence, the correlation of the molar fractions has a kinetic reason. However, in the Co–Ni–Cu system, Co and Cu have very low equilibrium miscibility and the deposition rate constants are presumably independent of each other. Therefore, the correlation of the codeposition rates is rather surprising. The contradiction can be resolved by assuming that fluctuation of the molar fractions, even in the case of a binary alloy, was caused by the hydrodynamic instability of the depleted electrolyte layer in the neighborhood of the cathode. In this case, if the natural convection is accelerated near the upward facing cathode, the transport rate of all reactant increases strictly at the same time. If the incorporation rate of several reactants is limited by the transport of the corresponding precursor ions, the correlated fluctuation of the codeposition rates can be easily elucidated.

Another tough question is what can cause the increase of the molar fraction of the preferentially deposited component(s) again after the nucleation zone. Several possibilities have to be considered:

1. The deposition rate of the main component of the alloys (in our case, Ni) becomes also partially mass transport limited. Hence, the limited supply of all reactant levels off the initial concentration changes. Nevertheless, this possibility is very unlikely due to the large difference in the concentrations of the ions of preferentially deposited minor and the major components.
2. There is a hidden kinetic reason for the increase of the molar fraction(s) of the minor component(s). The deposition would tend to be of oscillating nature, but the oscillation is damped by the depletion of the electrolyte so fast that only the first wave is detected. This opportunity is also unlikely because the same trend in the composition depth profile was seen for many alloying element independently of the codeposition mode.
3. The depleted layer near the cathodes behaves at the beginning of the deposition similar to an overcooled liquid in the sense that temporarily the thickness of the depleted layer can be thicker than in the steady state. After the initial zone, as the transport and natural convection near the cathode is stabilized, the diffusion

layer shrinks a bit, which leads to a larger concentration gradient and consequently a larger ion transport rate.

It is not possible to decide which mechanism is responsible for the increase of the molar fraction of the preferentially deposited minor component after the nucleation zone. Several other methods like an in situ study of the concentration of the electrolyte components by a beam deflection method, the study of the evolution of the deposit surface roughness, and the digital simulation of the kinetic models for various codeposition modes should be used to solve this problem.

Finally, it has to be mentioned shortly that in case of the normal codeposition mode (i.e., for Ni–Cu and Ni–Cd alloys), the partial current density of the preferentially deposited minority alloy component was much smaller than expected from the deposition rate of this component when it was present alone. It seems that the codeposition of the minority alloy component was suppressed in these cases. This result draws the attention to that the normal codeposition does not mean at all that the more noble metal is codeposited at the same rate as in the absence of the alloying element. This may have various reasons. It is possible that kinetic factors play a role in the suppression of the Cu or Cd codeposition, i.e., the Ni^{2+} ions being present in a much larger concentration simply block the active sites. For the Ni–Cd system, the suppression of the Cd deposition may also be caused by thermodynamic reasons due to the lack of a stable Cd–Ni phase with low Cd concentration.

Multilayer samples

Co–Cu/Cu multilayer samples were used to study the composition depth profile functions with the reverse sputtering direction. The solution for the deposition of Co–Cu/Cu multilayers contained the following components: $CoSO_4$ (0.80 mol/dm^3), $CuSO_4$ (0.015 mol/dm^3), H_3BO_3 (0.20 mol/dm^3), and $(NH_4)_2SO_4$ (0.20 mol/dm^3). The Co-rich layers were deposited at −60 mA/cm^2 constant current density with a predefined pulse duration, and the Cu layers were produced at −0.6 V constant potential by monitoring the charge passed through the cell. Various multilayer samples with a 10- to 20-nm periodicity were prepared, and all samples were covered with a Ni supporting layer.

The results obtained with the conventional and reverse sputtering directions were compared [29]. In both cases, it could be seen in the composition depth profile functions (Fig. 18) that the samples do exhibit the periodicity calculated from the parameters of the electrodeposition, but the oscillation amplitude of the Co and Cu signals in the depth profile functions were different. For a multilayer with 10 nm periodicity, the intensity oscillation for Co and Cu

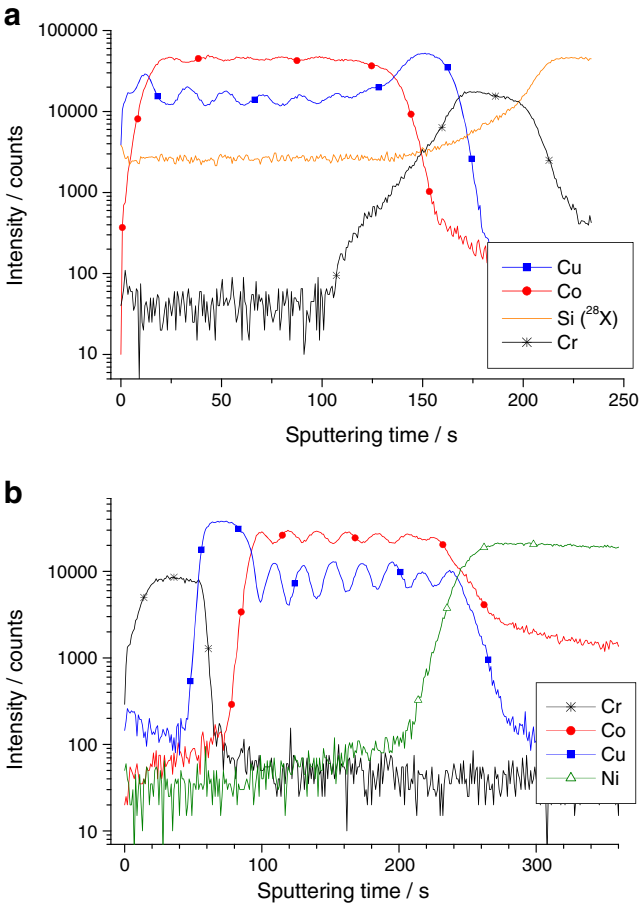

Fig. 18 Comparison of the composition depth profile of Si/Cr(20 nm)/Cu(20 nm)//[Co(5.4 nm)/Cu(4.4 nm)]×7 samples as measured with conventional sputtering direction on the substrate (**a**) and after covering a Ni layer and detached from the substrate and measured with the reverse sputtering direction (**b**). Reproduced with the permission of The Electrochemical Society [29]

were as low as 10% and 38%, respectively, when the sputtering was performed in the conventional mode. However, when the reverse technique was applied, these values raised to 24% and 60%, respectively. Hence, it was shown that the reverse sputtering direction yields a better resolution of electrodeposited layers when the sputtering is started from the smooth backside surface.

The problem of interface widening during sputtering-based DPA methods has long been known. The theoretical relationships for both the interface broadening and the signal deconvolution procedure were formulated several decades ago [66], although there was no tool at that time either to measure the sputtering-induced roughness or to perform the computation-demanding deconvolution procedure. Nowadays, a common approach is [67] to take into account the sputtering-induced roughness by assuming infinitely abrupt interfaces, on the one hand, and a Gaussian function with increasing full width at half maximum to describe the broadening, on the other hand. It is also widely

accepted that the full width at half maximum of the apparently faded interface is approximated with a power function [67]. The most accurate approach is the calculation of the experimentally measured profile (y) with a convolution of the real depth profile (y') and the depth resolution function (g) [68]:

$$y(x) = \int_{-\infty}^{\infty} y'(x')g(x - x')dx'$$

where x is the sputtering depth. For electrodeposited multilayers, the roughening during the deposition process is much more significant than the sputtering-induced roughness of the same specimen during DPA. Hence, the same relationships can be used, replacing the sputtering-induced roughness with the surface roughness of the ED samples [29]. An advantage of this approach is that the surface roughness of ED samples can be measured with atomic force microscopy. For the thickness range studied, the depth resolution function could be fitted with a Gaussian function (G), and hence, the calculation could be easily done with a numerical algorithm. The calculation is hence based on the following equation [29]:

$$y(x) = \int_{-\infty}^{\infty} y'(x')G(x - x', \sigma(x))dx'$$

where σ (x)is the width of the Gaussian function, being also a function of the depth. The latter parameter can be measured with AFM, and hence, the experimental depth profile can be calculated.

Figure 19 shows two corresponding curves. The top part of the figure indicates the width of the surface height distribution function (symbols) and a continuous function that was used for the depth profile calculation. The bottom part of the same figure shows the result of the DPA study (symbols) in comparison with the result of the calculation as described above. The calculation shows excellent agreement with the experiments. The detailed discussion of the multilayer analysis can be found in [29].

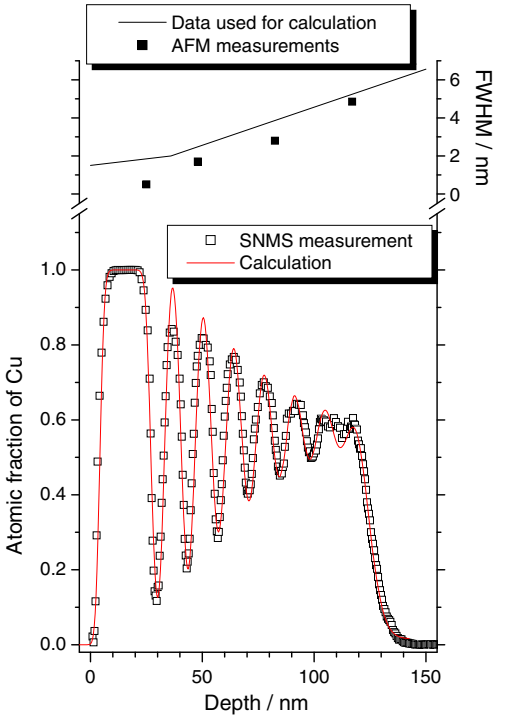

Fig. 19 Comparison of the measured and calculated depth profile data for a sample with Cr(5 nm)/Cu(20 nm)//[Co(7.0 nm)/Cu(5.5 nm)]×7//Ni structure. *Top part*: the mean AFM roughness measured at the same total sample thickness (*symbols*) and the roughness vs. depth function (*continuous line*) used to achieve the best fit of the calculation of the experimental reverse depth profile data. Reproduced with the permission of The Electrochemical Society [29]

Summary and outlook

It has been shown that the reverse approach of the composition depth profile analysis combined with the application of the advanced SNMS method is very useful for the analysis of electrodeposited metallic specimens. In particular, one can obtain an unprecedented insight into the in-depth component distribution in near-substrate zone of the deposit. It has been obtained for many nickel alloys that a spontaneous composition modulation occurs in the near-substrate zone of the deposit, although a constant current was applied and no intentional modulation was applied by, e.g., the modulation of the cathodic current. The initial zone in which the spontaneous modulation decays was found to be about 150 nm. Hence, the homogeneity of the alloys studied could not be ensured for thicknesses lower than this distance. Since the production of ultrathin layers become more and more important nowadays, a special care has to be taken when electrodeposited alloys thinner than 150 nm have to be applied.

When two preferentially deposited alloy components were present, the molar fraction maxima of these metals in the deposit followed the order of the deposition preference. Interestingly, a correlation was found between the molar fractions of the preferentially deposited alloying elements. The explanation of this correlation deserves particular attention in the future.

The reverse DPA proved to be useful for the analysis of multilayers as well. A quantitative method was developed to take into account the change of the surface roughness of the deposit during the calculation of the DPA results.

The limitations of the reverse DPA method cannot be fully established at present. Due to the vulnerability of the substrate layers on the Si wafer, deposits with large internal

stress cannot be grown to a sufficiently large thickness. For instance, Fe–Co–Ni alloys deposited with a citrate-stabilized bath or Fe–Ni–Sn alloys produced with a gluconate bath were so stressed that the Cr/Cu layer was peeled off from the Si wafer when the deposit thickness reached 100–300 nm. Therefore, the internal stress is one of the limiting factors influencing the applicability of the reverse DPA method.

There are various groups of electrodeposited alloys whose composition depth profile could be interesting. Since Zn is preferentially deposited together with the iron group metal, one can expect a Zn enrichment in the near-substrate zone of electrodeposited Zn–iron group metal alloys. Since the codeposition process of Zn with Fe, Co, and Ni is also classified as being anomalous, the composition depth profile analysis could reveal general aspects of the anomalous codeposition. Similarly, the reverse DPA method is yet to be tested for other codeposition modes like irregular or induced codeposition.

Another important question to be clarified is whether pulse plating is suitable to suppress the large composition modulation in the near-substrate zone of ED alloys. Since pulse plating is generally considered as a flexible method for adjusting ED alloy composition and grain size, the reverse DPA of pulse-plated alloys may reveal new features of the pulsed electrodeposition as well.

Acknowledgments K. Neuróhr and L. Péter acknowledge Prof. György Inzelt for his support and his outstanding activity in the education of electrochemistry. The present work was funded by the Hungarian Scientific Research Fund (OTKA) through grant # NN 79846.

References

1. Hightower A, Koel B, Felter T (2009) Electrochim Acta 54:1777–1783
2. Palacio C, Ocón P, Herrasti P, Díaz D, Arranz A (2003) J Electroanal Chem 545:53–58
3. Kossoy E, Khoptiar Y, Cytermann C, Shemesh G, Katz H, Sheinkopf H, Cohen I, Eliaz N (2008) Corros Sci 50:1481–1491
4. Stangl M, Acker J, Oswald S, Uhlemann M, Gemming T, Baunack S, Wetzig K (2007) Microel Eng 84:54–59
5. Favry E, Frederich N, Meunier A, Omnes L, Jomard F, Etcheberry A (2008) Electrochim Acta 53:7004–7011
6. Martín AJ, Chaparro AM, Gallardo B, Folgado MA, Daza L (2009) J Power Sources 192:14–20
7. Bardi U, Caporali S, Chenakin SP, Lavacchi A, Miorin E, Pagura C, Tolstogouzov A (2006) Surf Coat Technol 200:2870–2874
8. Nakanishi S, Sakai S, Nagai T, Nakato Y (2005) J Phys Chem B 109:1750–1755
9. Padhi D, Gandikota S, Nguyen HB, McGuirk C, Ramanathan S, Yahalom J, Dixit G (2003) Electrochim Acta 48:935–943
10. Gómez E, Pllicier E, Vallés E (2003) J Appl Electrochem 33:245–252
11. Dulal SMSI, Yun HJ, Shin CB, Kim CK (2009) Appl Surf Sci 255:5795–5801
12. Koo HC, Cho SK, Kwon OJ, Suh MW, Im Y, Kim JJ (2009) J Electrochem Soc 156:D236–D241
13. Pisarek M, Janik-Czachor M, Donten M (2008) Surf Coat Technol 202:1980–1984
14. Sakai S, Nakanishi S, Nakato Y (2006) J Phys Chem B 110:11944–11949
15. Shimizu K, Brown GM, Habazaki H, Kobayashi K, Skeldon P, Thompson GE, Wood GC (2001) Corros Sci 43:199–205
16. Egberts P, Brodersen P, Hibbard GD (2006) Mat Sci Eng A 441:336–341
17. Ahadian MM, Irajizad A, Nouri E, Ranjbar M, Dolati A (2007) J Alloy Comp 443:81–86
18. Ranjbar M, Ahadian MM, Irajizad A, Dolati A (2006) Mat Sci Eng B 127:17–21
19. Angeli J, Kaltenbrunner T, Androsch (1991) Fresenius J Anal Chem 341:140–144
20. Csik A, Vad K, Tóth-Kádár E, Péter (2009) Electrochem Commun 11:1289–1291
21. Péter L, Csik A, Vad K, Tóth-Kádár E, Pekker Á, Molnár G (2010) Electrochim Acta 55:4734–4741
22. Iselt D, Gaitzsch U, Oswald S, Fähler S, Schultz L, Schlörb H (2011) Electrochim Acta 56:5178–5183
23. Leistner K, Thomas J, Baunack S, Schlörb H, Schultz L, Fähler S (2005) J Magn Magn Mater 290–291:1270–1273
24. Lukaszewski M, Klimek K, Czerwinski A (2009) J Electroanal Chem 637:13–20
25. Papadimitriou S, Armyanov S, Valova E, Hubin A, Steenhaut O, Pavlidou E, Kokkinidis G, Sotiropoulos S (2010) J Phys Chem C 114:5217–5223
26. Gupta D, Nayak AC, Sharma M, Singh RR, Kulkarni SK, Pandey RK (2006) Thin Solid Films 513:187–192
27. Péter L, Katona GL, Berényi Z, Vad K, Langer GA, Tóth-Kádár E, Pádár J, Pogány L, Bakonyi I (2007) Electrochim Acta 53:837–845
28. Katona GL, Berényi Z, Péter L, Vad K (2008) Vacuum 82:270–273
29. Bartók A, Csik A, Vad K, Molnár G, Tóth-Kádár E, Péter L (2009) J Electrochem Soc 156:D253–D260
30. Csik A, Vad K, Langer GA, Katona GL, Tóth-Kádár E, Péter L (2010) Vacuum 84:141–143
31. Hernández-Vélez M, Pirota KL, Pászti F, Navas D, Climent A, Vázquez M (2005) Appl Phys A 80:1701–1706
32. Vázquez M, Hernández-Vélez M, Pirota K, Asenjo A, Navas D, Velázquez J, Vargas P, Ramos C (2004) Eur Phys J B 40:489–497
33. Singh S, Basu S, Ghosh SK (2009) Appl Surf Sci 255:5910–5916
34. Takahashi M, Kojima M, Sato S, Ohnisi N, Nishiwaki A, Wakita K, Miyuki T, Ikeda S, Muramatsu Y (2004) J Appl Phys 96:5582–5587
35. Kang SH, Kim YK, Choi DS, Sung YE (2006) Electrochim Acta 51:4433–4438
36. Calixto ME, Sebastian PJ (2000) Solar Energy Materials & Solar Cells 63:335–345
37. Nauer M, Ernst K, Kautek W, Neumann-Spallart M (2005) Thin Solid Films 489:86–93
38. Rogers KD, Wood DA, Painter JD, Lane DW, Ozsan ME (2000) Thin Solid Films 361–362:234–238
39. Seipel B, Nadarajah A, Wutzke B, Könenkamp R (2009) Mater Lett 63:736–738
40. Lu M, Cheng H, Yang Y (2008) Electrochim Acta 53:3539–3546
41. Cheng H, Zhu C, Lu M, Yang Y (2007) J Power Sources 173:531–537
42. Saito Y, Rahman MK (2007) J Power Sources 174:877–882
43. Kowalski D, Aoki Y, Habazaki H (2009) Angew Chem Int Ed 48:7582–7585, Supporting information
44. Shimizu K, Habazaki H, Skeldon P, Thompson GE, Wood GC (2000) Electrochim Acta 45:1805–1809

45. Benzakour J, Derja A (1997) J Electroanal Chem 437:119–124
46. Crossland AC, Thompson GE, Smith CJE, Habazaki H, Shimizu K, Skeldon P (1999) Corros Sci 41:2053–2069
47. Wener Z, Jaskiewicz A, Pisarek M, Janik-Czachor M, Barlak M (2005) Z Phys Chem 219:1461–1479
48. Suleiman A, Hashimoto T, Skeldon P, Thompson GE, Echeverria F, Graham MJ, Sproule GI, Moisa S, Habazaki H, Bailey P, Noakes TCQ (2008) Corr Sci 50:1353–1359
49. Cho EA, Ahn SJ, Kwon HS (2005) Electrochim Acta 50:3383–3389
50. Mohanty US, Lin KL (2007) J Mater Res 22:2573–2581
51. Sziráki L, Cziráki A, Vértesy, Kiss L, Ivanova V, Raichevski G, Vitkova S, Marinova S (1999) J Appl Electrochem 29:927–937
52. Janik-Czachor M, Pisarek M (2009) In: Pyun SI, Lee JW (eds) Modern aspects of electrochemistry 46, Chapter 3. New York, Springer, pp 175–230
53. Sosa E, Cabrera-Sierra R, Oropeza MT, Hernández F, Casillas N, Tremont R, Cabrera C, González I (2003) Electrochim Acta 48:1665–1674
54. Kowalski D, Ueda M, Ohtsuka T (2007) Corros Sci 49:3442–3452
55. Kazeminezhad I, Blythe HJ, Schwarzacher W (2001) Appl Phys Lett 78:1014–1016
56. Kazeminezhad I, Schwarzacher W (2001) J Magn Magn Mater 226:1650–1652
57. Kazeminezhad I, Schwarzacher W (2002) J Magn Magn Mater 240:467–468
58. Kazeminezhad I, Schwarzacher W (2004) J Solid State Electrochem 8:187–189
59. Massalski TB (ed) (1996) Binary alloy phase diagrams, second edition plus updates on CD-ROM. ASM International, Materials Park
60. Mohanty US, Tripathy BC, Singh P, Das SC (2004) J Electroanal Chem 566:47–52
61. Mohanty US, Tripathy BC, Singh P, Das SC (2002) J Electroanal Chem 526:63–68
62. Liu X, Zangari G, Shen L (2000) J Appl Phys 87:5410–5412
63. Tabakovich I, Inturi V, Riemer S (2002) J Electrochem Soc 149: C18–C22
64. Perez L, Attenborough K, De Boeck J, Celis JP, Aroca C, Sánchez P, López E, Sánchez MC (2002) J Magn Magn Mater 242–245:163–165
65. Liu X, Zangari G, Shamsuzzoha M (2003) J Electrochem Soc 150:C159–C168
66. Van Cittert PH (1931) Z Phys 69:298
67. Escobar Galindo R, Albella JM (2008) Spectrochim Acta B 63:422–430
68. Escobar Galindo R, Forniés E, Albella JM (2005) J Anal At Spectrom 20:116–1120